Available online at www.sciencedirect.com
ScienceDirect
Comput. Methods Appl. Mech. Engrg. 296 (2015) 1–17
Computer methods in applied mechanics and engineering
www.elsevier.com/locate/cma

A gradient-based shape optimization scheme using an interface-enriched generalized FEM

Ahmad R. Najafi[a,b], Masoud Safdari[c], Daniel A. Tortorelli[a], Philippe H. Geubelle[c,b,*]

[a] *Department of Mechanical Science and Engineering, University of Illinois at Urbana–Champaign, 1206 West Green Street, Urbana, IL 61801, USA*

[b] *Beckman Institute for Advanced Science and Technology, University of Illinois at Urbana–Champaign, 405 North Mathews Avenue, Urbana, IL 61801, USA*

[c] *Department of Aerospace Engineering, University of Illinois at Urbana–Champaign, 104 South Wright Street, Urbana, IL 61801, USA*

Received 13 January 2015; received in revised form 21 July 2015; accepted 27 July 2015
Available online 3 August 2015

Abstract

A gradient-based shape optimization scheme using an Interface-enriched Generalized Finite Element Method (IGFEM) is presented wherein the design geometry is projected onto a fixed mesh and the IGFEM is used for analysis. This approach eliminates the mesh distortion present in conventional Lagrangian shape optimization methods, as well as the need for remeshing. An analytical sensitivity analysis using both the adjoint or direct approaches is presented to compute derivatives of the objective and constraint functions. Due to the fixed nature of the mesh, the so-called design velocity field only needs to be computed on the structure boundary/interface. A comparison between IGFEM- and conventional FEM-based shape optimization schemes is presented, showing an improved precision for the IGFEM approach. Finally, we solve various numerical examples to demonstrate the capability of the method including the computational design of particulate and microvascular composites.

Keywords: Gradient-based shape optimization; GFEM; Fixed grid; Analytical sensitivity analysis

1. Introduction

In shape optimization studies, the position of each material point in the domain or minimally on the boundary and material interfaces is a function of the shape design variables [1]. Therefore, initial finite-element-based shape optimization studies used the nodal coordinates as the design variables [2]. However, this approach was discarded due to mesh irregularities and the excessive number of design parameters [3,4]. Several methods including mesh parameterizations [5–8] and natural design variables [9,10] were then suggested to overcome these problems. Filtering techniques were also proposed to ensure boundary smoothness [11–14]. However, these Lagrangian shape optimization approaches still face drawbacks. Namely, large shape changes during the optimization process cause excessive

* Corresponding author at: Department of Aerospace Engineering, University of Illinois at Urbana–Champaign, 104 South Wright Street, Urbana, IL 61801, USA. Tel.: +1 217 244 7648; fax: +1 217 244 0720.
E-mail addresses: geubelle@uiuc.edu, geubelle@illinois.edu (P.H. Geubelle).

http://dx.doi.org/10.1016/j.cma.2015.07.024
0045-7825/

mesh distortion which deteriorates the accuracy of the finite element solution [15,16]. Although adaptive remeshing can alleviate this issue, it increases the complexity and computational cost [4,15–17].

In contrast to Lagrangian methods, Eulerian approaches mitigate mesh distortion problems by projecting the design domain over a fixed mesh [15,16,18,19]. These Eulerian methods incorporate mesh-free [20,21], fictitious domain [15,17,19,22,23], material perturbation [24], level-set [16,18,25,26], and the generalized/extended finite element methods (G/XFEM) [16,27–31].

In this paper, we present an Eulerian based shape optimization scheme that incorporates the Interface-enriched Generalized Finite Element Method (IGFEM) [32,33]. Like its G/XFEM counterparts, the IGFEM is formulated on a fixed mesh, thereby eliminating the mesh distortion problems associated with Lagrangian shape optimization schemes. The proposed method optimizes the geometric parameters that explicitly define structural boundary/interfaces, in contrast with level-set methods, which solve a partial differential equation, e.g., the Hamilton–Jacobi equation, to update the interface.

A crucial ingredient in gradient-based optimization is the sensitivity analysis that computes the derivatives of the objective and constraint functions with respect to the design variables. The computation of the design sensitivities has been the topic of multiple studies [1,34–38], which can be classified in four broad categories: (i) overall or global finite differences, (ii) discrete derivatives or discretize then differentiate, (iii) continuum derivatives or differentiate then discretize, and (iv) computational or automatic differentiation [38]. The latter three methods encompass either direct or adjoint variants. Ultimately the choice of the method is based on designed level of desired accuracy, computational efficiency, and implementation effort.

To perform the shape design sensitivity analysis, the boundary/interface nodes are parameterized by the shape design variables [15,35]. A key component of any sensitivity analysis is the so-called *design velocity field*, i.e, the derivative of the material point locations with respect to the design parameters. Due to the stationary nature of the non-conforming mesh in the IGFEM shape optimization scheme, the design velocity field is only needed at the boundary/material interface nodes to obtain the design sensitivity. In other words, in the present method, only the enriched nodes on the boundary/interface move, appear or disappear during the shape optimization process.

In this study, a discrete derivative sensitivity analysis (ii) is implemented to avoid the technical difficulties encountered in the finite difference or semi-analytical schemes [16,27]. Problems in those methods occur when the boundary is close to a node. In these situations the boundary may move to another element during the design perturbation step, resulting in changes of the mesh topology, making the differentiation of the stiffness matrix and load vector problematic. The proposed analytical method has no such problem. However, as is the case in all G/XFEM methods, the sensitivity analysis introduced in this study encounters a problem when the material interfaces pass through a node. In these situations, only the directional derivatives of the stiffness matrix and load vector can be evaluated. This problem is further described in Section 3.

The proposed approach extends the shape derivative method presented by [26] to the case of multiphase material interfaces. A related analytical sensitivity study based on XFEM was presented in [31]. However, in that study, only design-independent loading was considered and the shape sensitivity analysis only included the derivative of element stiffness matrices. In contrast, the sensitivity analysis developed in the present study considers derivatives of both stiffness matrices and force vectors. The latter involves shape derivatives of the FEM shape functions, which, to the best of our knowledge, have been neglected in previous Eulerian-based methods.

The remaining part of this manuscript is organized as follows: in the next section, a brief introduction to the IGFEM is presented. In Section 3, the optimization problem and the sensitivity analysis are described. The optimization algorithm is presented in Section 4, followed, in Section 5, by examples which illustrate the proposed method.

2. Interface-enriched finite element method (IGFEM)

A recent addition to the family of Generalized/Extended Finite Element Methods (G/XFEM), the IGFEM was introduced by Soghrati et al. [32,33] to capture gradient discontinuities present along material interfaces using non-conforming meshes. In the IGFEM, the enrichment functions and the associated generalized dofs are created by inserting nodes at the intersections of the interface with the boundaries of the non-conforming elements [32]. This contrasts with conventional G/XFEM where the generalized dofs are associated with duplicated nodes of the non-conforming elements [39,40]. However, similar to G/XFEM, for integration purposes the IGFEM relies on the subdomains decomposition that conforms to the material interface in the enriched elements. This contrasts other

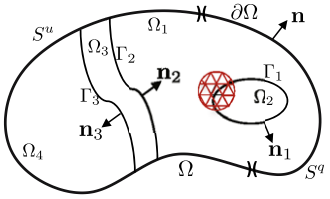

Fig. 1. Schematic of the geometry and boundary conditions. A subset of the non-conforming finite element mesh is also shown.

approaches such as the finite cell method [41–43], where integration over bi-material cells is performed using adaptive composite Gaussian quadrature schemes wherein the integration sub-cells do not conform to the interface.

To illustrate the IGFEM formulation, we consider its application to steady-state heat conduction problems, although some of the examples provided in Section 5 also involve structural applications. As shown in Fig. 1, the domain $\Omega = \cup_{i=1}^{N_\Omega} \Omega_i \subset R^2, \cap_{i=1}^{N_\Omega} \Omega_i = \emptyset$ with closure $\bar{\Omega}$ is bounded by $\partial\Omega = \bar{\Omega} - \Omega$ with outward normal vector $\mathbf{n}$, where N_Ω is the number of subdomains $\Omega_i, i = 1, 2, \ldots, N_\Omega$. The boundary $\partial\Omega$ is split into two complementary subsets S^q and S^u, i.e., $\partial\Omega = S^u \cup S^q$ and $S^u \cap S^q = \emptyset$, over which heat flux q and temperature $\bar{u}$ are prescribed. It is assumed that the material interfaces are smooth and are defined by $\Gamma = \cup_{i=1}^{N_\Gamma} \Gamma_i \subset R$ and satisfy $\cap_{i=1}^{N_\Gamma} \Gamma_i = \emptyset$, where N_Γ is the number of interfaces. The normal vector on each material interface Γ_i is denoted as $\mathbf{n}_i$.

In the IGFEM, we discretize the domain $\Omega \approxeq \Omega_\mathrm{h}$ with a mesh that does not conform to the material interfaces. The temperature field in each element intersected by an interface takes the form [32,44]

$$u^h(\mathbf{X}) = \sum_{i=1}^{n} N_i(\mathbf{X})\, u_i + \sum_{j=1}^{n_\psi} \psi_j(\mathbf{X})\, \alpha_j = \begin{bmatrix} \mathbf{N}(\mathbf{X}) & \boldsymbol{\Psi}(\mathbf{X}) \end{bmatrix} \begin{Bmatrix} \mathbf{U} \\ \mathbf{A} \end{Bmatrix}, \tag{1}$$

where the first sum on the right hand side of (1) represents the classical finite element approximation with the n standard finite element shape functions $N_i(\mathbf{X})$ and the standard nodal dofs u_i, and the second sum represents the augmented contribution with the n_ψ enrichment functions $\psi_j(\mathbf{X})$ and their associated generalized dofs α_j. In the IGFEM, generalized dofs are assigned to the interface nodes, which are inserted to the locations where the interface intersects the element edges.

To evaluate enrichment functions $\psi_j(\mathbf{X})$, consider an enriched (parent) element with domain Ω_e that is divided into two subdomains $\Omega_e^{(1)}$ and $\Omega_e^{(2)}$ by the internal interface (Fig. 2). These subdomains serve as the integration (children) elements, wherein the enrichment functions corresponding to the interface nodes E_1 and E_2 are the standard Lagrangian shape functions defined piecewise over the integration elements as

$$\begin{aligned} \psi_1(\mathbf{X}) &= \begin{cases} \psi_1^{(1)}(\mathbf{X}) = N_1^{(1)}(\mathbf{X}) & \forall \mathbf{X} \in \Omega_e^{(1)} \\ \psi_1^{(2)}(\mathbf{X}) = N_2^{(2)}(\mathbf{X}) & \forall \mathbf{X} \in \Omega_e^{(2)}, \end{cases} \\ \psi_2(\mathbf{X}) &= \begin{cases} \psi_2^{(1)}(\mathbf{X}) = N_2^{(1)}(\mathbf{X}) & \forall \mathbf{X} \in \Omega_e^{(1)} \\ \psi_2^{(2)}(\mathbf{X}) = N_1^{(2)}(\mathbf{X}) & \forall \mathbf{X} \in \Omega_e^{(2)}. \end{cases} \end{aligned} \tag{2}$$

Since the standard Lagrangian shape functions are used to construct the enrichment functions $\psi_j(\mathbf{X})$, by definition they vanish at the nodes and the edges of the element that do not intersect the interface. For example, for an enriched 3-node triangular element Ω_e, $\mathbf{N}(\mathbf{X})$ appearing in (1) is a 1×3 row vector, composed of the standard Lagrangian shape functions associated with Ω_e, while $\boldsymbol{\Psi}(\mathbf{X})$ is a 1×2 row vector, containing the shape functions ψ_1 and ψ_2 corresponding to the enriched interface nodes E_1 and E_2, as shown in Fig. 2.

As usual, we use the derivatives of the shape functions to approximate the thermal gradients as

$$\frac{\partial u^h(\mathbf{X})}{\partial \mathbf{X}} = \begin{bmatrix} \dfrac{\partial \mathbf{N}(\mathbf{X})}{\partial \mathbf{X}} & \dfrac{\partial \boldsymbol{\Psi}(\mathbf{X})}{\partial \mathbf{X}} \end{bmatrix} \begin{Bmatrix} \mathbf{U} \\ \mathbf{A} \end{Bmatrix} = \begin{bmatrix} \mathbf{B}_N(\mathbf{X}) & \mathbf{B}_\psi(\mathbf{X}) \end{bmatrix} \begin{Bmatrix} \mathbf{U} \\ \mathbf{A} \end{Bmatrix}, \tag{3}$$

where the definition of $\mathbf{B}_N$ and $\mathbf{B}_\psi$ are self evident.

For heat conduction problems, the implementation of the IGFEM results in the following system of equations:

$$\mathbb{K}\mathbb{U} = \mathbb{F}, \tag{4}$$

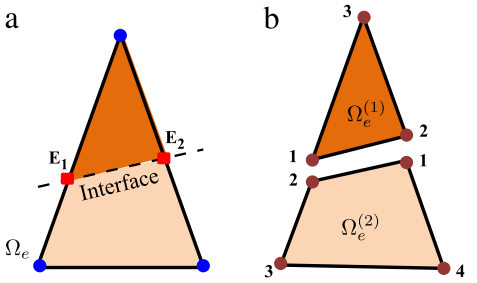

Fig. 2. Creation of integration elements: (a) schematic of an enriched element, which is cut by an interface; (b) two integration elements used to compute the shape functions.

where $\mathbb{U}$ is the global nodal solution vector, $\mathbb{F}$ denotes the global nodal force vector, and $\mathbb{K}$ is the global stiffness matrix. As usual, $\mathbb{K}$ is assembled from the element stiffness matrices $\mathbf{K}^e$,

$$\mathbf{K}^e = \int_{\Omega_e} \mathbb{B}^T(\mathbf{X})\, \mathbb{D}(\mathbf{X})\, \mathbb{B}(\mathbf{X})\, d\Omega, \tag{5}$$

where $\mathbb{D}$ is the thermal conductivity matrix, and

$$\mathbb{B}(\mathbf{X}) = \left[\mathbf{B}_N(\mathbf{X}) \quad \mathbf{B}_\psi(\mathbf{X})\right]. \tag{6}$$

Substituting (6) into (5) results in

$$\mathbf{K}^e = \begin{bmatrix} \mathbf{K}^e_{uu} & \mathbf{K}^e_{u\alpha} \\ \mathbf{K}^e_{\alpha u} & \mathbf{K}^e_{\alpha\alpha} \end{bmatrix}, \tag{7}$$

where

$$\begin{aligned}
\mathbf{K}^e_{uu} &= \sum_{i=1}^{2} \int_{\Omega_e^{(i)}} \mathbf{B}_N^T(\mathbf{X})\, \mathbb{D}(\mathbf{X})\, \mathbf{B}_N(\mathbf{X})\, d\Omega, \\
\mathbf{K}^e_{u\alpha} &= \sum_{i=1}^{2} \int_{\Omega_e^{(i)}} \mathbf{B}_N^T(\mathbf{X})\, \mathbb{D}(\mathbf{X})\, \mathbf{B}_\psi(\mathbf{X})\, d\Omega, \\
\mathbf{K}^e_{\alpha u} &= \sum_{i=1}^{2} \int_{\Omega_e^{(i)}} \mathbf{B}_\psi^T(\mathbf{X})\, \mathbb{D}(\mathbf{X})\, \mathbf{B}_N(\mathbf{X})\, d\Omega, \\
\mathbf{K}^e_{\alpha\alpha} &= \sum_{i=1}^{2} \int_{\Omega_e^{(i)}} \mathbf{B}_\psi^T(\mathbf{X})\, \mathbb{D}(\mathbf{X})\, \mathbf{B}_\psi(\mathbf{X})\, d\Omega.
\end{aligned} \tag{8}$$

The above holds for the elements that are intersected by the interface; for the all the other elements $\mathbf{B}_\psi = 0$ and the element stiffness matrix takes the usual form. Similarly, the global nodal force vector $\mathbb{F}$ in (4) is assembled from the element nodal force vector $\mathbf{F}^e$,

$$\mathbf{F}^e = \int_{\Omega_e} \mathbb{N}^T(\mathbf{X})\, Q(\mathbf{X})\, d\Omega + \int_{\Gamma_e \cap S^q} \mathbb{N}^T(\mathbf{X})\, q(\mathbf{X})\, d\Gamma, \tag{9}$$

where Q and q are the heat source and applied heat flux defined on element Ω_e and element boundary $\Gamma_e \cap S^q$, respectively, and $\mathbb{N}$ is the element shape function vector, given as

$$\mathbb{N}(\mathbf{X}) = \left[\mathbf{N}(\mathbf{X}) \quad \mathbf{\Psi}(\mathbf{X})\right]. \tag{10}$$

Substituting (10) into (9) leads to

$$\mathbf{F}^e = \begin{bmatrix} \mathbf{F}^e_u \\ \mathbf{F}^e_\alpha \end{bmatrix}, \tag{11}$$

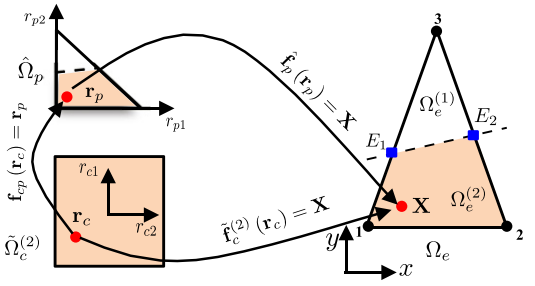

Fig. 3. Mappings used to evaluate the shape functions at an integration point $\mathbf{X}$. $\tilde{f}_c^{(2)}(\mathbf{r}_c)$ is the mapping from the master element $\tilde{\Omega}_c^{(2)}$ to the integration element $\Omega_e^{(2)}$, whereas $\hat{f}_p(\mathbf{r}_p)$ maps the master element $\hat{\Omega}_p$ to the element Ω_e (triangle $1-2-3$), and $\mathbf{f}_{cp}(\mathbf{r}_p)$ is a composite mapping defined as $\hat{\mathbf{f}}_p^{\downarrow} \circ \tilde{\mathbf{f}}_c^{(2)}$.

where

$$\mathbf{F}_u^e = \sum_{i=1}^{2} \left\{ \int_{\Omega_e^{(i)}} \mathbf{N}^T(\mathbf{X})\, Q(\mathbf{X})\, d\Omega + \int_{\Gamma_e^{(i)} \cap S^q} \mathbf{N}^T(\mathbf{X})\, q(\mathbf{X})\, d\Gamma \right\},$$
$$\mathbf{F}_\alpha^e = \sum_{i=1}^{2} \left\{ \int_{\Omega_e^{(i)}} \mathbf{\Psi}^T(\mathbf{X})\, Q(\mathbf{X})\, d\Omega + \int_{\Gamma_e^{(i)} \cap S^q} \mathbf{\Psi}^T(\mathbf{X})\, q(\mathbf{X})\, d\Gamma \right\}. \tag{12}$$

As with the element stiffness matrix, $\mathbf{F}_\alpha^e \neq 0$ for only the intersected elements.

We use a standard isoparametric FEM wherein the integrals that define the element stiffness matrices and load vectors are computed via Gaussian quadratures. However, this requires special care over the enriched elements due to discontinuity of the interpolation, as the enriched element Ω_e must be split into its two integration elements $\Omega_e^{(1)}$ and $\Omega_e^{(2)}$. To this end and without loss of generality, we refer the reader to Fig. 3, which illustrates the required isoparametric mappings for evaluating the shape functions over the integration element $\Omega_e^{(2)}$ of Fig. 2. As seen in Fig. 3, a master integration element $\tilde{\Omega}_c^{(2)}$ is the image of the integration element $\Omega_e^{(2)}$ under the map $\tilde{\mathbf{f}}_c^{(2)}$, i.e., $\tilde{\mathbf{f}}_c^{(2)} : \tilde{\Omega}_c^{(2)} \to \Omega_e^{(2)}$ such that

$$\begin{aligned} \mathbf{X} &= \tilde{\mathbf{f}}_c^{(2)}(\mathbf{r}_c) \\ &= \tilde{\mathbf{N}}_c^{(2)}(\mathbf{r}_c)\, \mathbf{X}_e^{(2)}, \end{aligned} \tag{13}$$

where $\mathbf{X}_e^{(2)}$ is a 4×2 matrix corresponding to the nodal coordinates of the integration element $\Omega_e^{(2)}$, and $\tilde{\mathbf{N}}_c^{(2)}$ is a 1×4 row vector containing the Lagrangian shape functions defined over the master element $\tilde{\Omega}_c^{(2)}$. Note that $\tilde{\mathbf{f}}_c^{(2)}(\mathbf{r}_c) = \mathbf{X}$ is a row vector and thusly its derivatives will be transpose that of the "usual" result.

Fig. 3 also shows that the enriched element Ω_e is the image of the master enriched element $\hat{\Omega}_p$ under the map $\hat{\mathbf{f}}_p$, i.e., $\hat{\mathbf{f}}_p : \hat{\Omega}_p^{(2)} \to \Omega_e$ such that

$$\begin{aligned} \mathbf{X} &= \hat{\mathbf{f}}_p(\mathbf{r}_p) \\ &= \hat{\mathbf{N}}_p(\mathbf{r}_p)\, \mathbf{X}_e, \end{aligned} \tag{14}$$

where $\mathbf{X}_e$ is a 3×2 matrix composed of the nodal coordinates of the enriched element Ω_e, and $\hat{\mathbf{N}}_p$ is a 1×3 vector containing the Lagrangian shape functions defined over the master element $\hat{\Omega}_p$.

Using the above mappings, the shape functions for integration element $\Omega_e^{(2)}$ takes the form

$$\begin{aligned} \mathbb{N}(\mathbf{X})\big|_{\mathbf{X}=\hat{\mathbf{f}}_p(\mathbf{f}_{cp}(\mathbf{r}_c))=\tilde{\mathbf{f}}_c^{(2)}(\mathbf{r}_c)} &= \left[\mathbf{N}\left(\mathbf{X}\big|_{\mathbf{X}=\hat{\mathbf{f}}_p(\mathbf{f}_{cp}(\mathbf{r}_c))}\right) \quad \mathbf{\Psi}^{(2)}\left(\mathbf{X}\big|_{\mathbf{X}=\tilde{\mathbf{f}}_c^{(2)}(\mathbf{r}_c)}\right) \right] \\ &= \left[\hat{\mathbf{N}}_p(\mathbf{r}_p)\big|_{\mathbf{r}_p=\mathbf{f}_{cp}(\mathbf{r}_c)} \quad \tilde{\mathbf{\Psi}}^{(2)}(\mathbf{r}_c) \right] \\ &= \left[\hat{\mathbf{N}}_p \circ \mathbf{f}_{cp}(\mathbf{r}_c) \quad \tilde{\mathbf{\Psi}}^{(2)}(\mathbf{r}_c) \right], \end{aligned} \tag{15}$$

where $\tilde{\mathbf{\Psi}}^{(2)}$ is a 1×2 row vector containing the Lagrangian shape functions in $\tilde{\mathbf{N}}_c^{(2)}$ which are associated to the enriched interface nodes E_1 and E_2, as shown in Figs. 2 and 3 and Eqs. (1) and (10). The shape function $\mathbf{\Psi}^{(2)}$ is evaluated at $\mathbf{X} \in \Omega_e^{(2)} \subset \Omega_e$ by using the mapping $\tilde{\mathbf{f}}_c^{(2)}$ from the master element $\tilde{\Omega}_c^{(2)}$ to the integration element $\Omega_e^{(2)}$, i.e., $\tilde{\mathbf{f}}_c^{(2)} : \tilde{\Omega}_c^{(2)} \to \Omega_e^{(2)}$ (Fig. 3). On the other hand, $\mathbf{N}$ is evaluated at $\mathbf{X} \in \Omega_e^{(2)} \subset \Omega_e$ using the mapping $\hat{\mathbf{f}}_p : \hat{\Omega}_p \to \Omega_e^{(2)}$. In performing integrations over $\Omega_e^{(2)}$, however, we require that $\mathbf{N}$ be evaluated via a map from $\tilde{\Omega}_c^{(2)}$. This is done by introducing the composite map $\mathbf{f}_{cp} = \hat{\mathbf{f}}_p^{\downarrow} \circ \tilde{\mathbf{f}}_c^{(2)} : \tilde{\Omega}_c^{(2)} \to \hat{\Omega}_p$ defined such that

$$\mathbf{r}_p = \mathbf{f}_{cp}\left(\mathbf{r}_c\right) = \hat{\mathbf{f}}_p^{\downarrow} \circ \tilde{\mathbf{f}}_c^{(2)}\left(\mathbf{r}_c\right) = \hat{\mathbf{f}}_p^{\downarrow}\left(\tilde{\mathbf{f}}_c^{(2)}\left(\mathbf{r}_c\right)\right), \tag{16}$$

where $\hat{\mathbf{f}}_p^{\downarrow} : \Omega_e^{(2)} \to \hat{\Omega}_p$ is the inverse map of $\hat{\mathbf{f}}_p$. Implementing the mappings presented in Fig. 3, the computation of $\mathbf{B}_N$ for integration element $\Omega_e^{(2)}$ over its corresponding master element $\hat{\Omega}_e^{(2)}$ takes the form

$$\begin{aligned} \mathbf{B}_N\left(\mathbf{X}\right)|_{\mathbf{X}=\hat{\mathbf{f}}_p(\mathbf{r}_p)} &= \frac{\partial}{\partial \mathbf{X}} \mathbf{N}\left(\mathbf{X}|_{\mathbf{X}=\hat{\mathbf{f}}_p(\mathbf{r}_p)}\right) \\ &= \hat{\mathbf{J}}_p^{-1}\left(\mathbf{r}_p\right) \frac{\partial \hat{\mathbf{N}}_p\left(\mathbf{r}_p\right)}{\partial \mathbf{r}_p}|_{\mathbf{r}_p=\mathbf{f}_{cp}(\mathbf{r}_c)}, \end{aligned} \tag{17}$$

where we define the derivatives

$$\frac{\partial \hat{\mathbf{N}}_p\left(\mathbf{r}_p\right)}{\partial \mathbf{r}_p} = \begin{bmatrix} \dfrac{\partial \hat{N}_{p1}\left(\mathbf{r}_p\right)}{\partial r_{p1}} & \dfrac{\partial \hat{N}_{p2}\left(\mathbf{r}_p\right)}{\partial r_{p1}} & \dfrac{\partial \hat{N}_{p3}\left(\mathbf{r}_p\right)}{\partial r_{p1}} \\ \dfrac{\partial \hat{N}_{p1}\left(\mathbf{r}_p\right)}{\partial r_{p2}} & \dfrac{\partial \hat{N}_{p2}\left(\mathbf{r}_p\right)}{\partial r_{p2}} & \dfrac{\partial \hat{N}_{p3}\left(\mathbf{r}_p\right)}{\partial r_{p2}} \end{bmatrix} \tag{18}$$

and where

$$\hat{\mathbf{J}}_p\left(\mathbf{r}_p\right) = \begin{bmatrix} \dfrac{\partial\left(\hat{\mathbf{f}}_p\left(\mathbf{r}_p\right)\right)_1}{\partial r_{p1}} & \dfrac{\partial\left(\hat{\mathbf{f}}_p\left(\mathbf{r}_p\right)\right)_2}{\partial r_{p1}} \\ \dfrac{\partial\left(\hat{\mathbf{f}}_p\left(\mathbf{r}_p\right)\right)_1}{\partial r_{p2}} & \dfrac{\partial\left(\hat{\mathbf{f}}_p\left(\mathbf{r}_p\right)\right)_2}{\partial r_{p2}} \end{bmatrix} = \frac{\partial \hat{\mathbf{f}}_p\left(\mathbf{r}_p\right)}{\partial \mathbf{r}_p} \tag{19}$$

is the Jacobian of mapping from the master element $\hat{\Omega}_p$ to the enriched element Ω_e. Similarly,

$$\begin{aligned} \mathbf{B}_{\psi}^{(2)}\left(\mathbf{X}\right)|_{\mathbf{X}=\tilde{\mathbf{f}}_c^{(2)}(\mathbf{r}_c)} &= \frac{\partial}{\partial \mathbf{X}} \mathbf{\Psi}^{(2)}\left(\mathbf{X}|_{\mathbf{X}=\tilde{\mathbf{f}}_c^{(2)}(\mathbf{r}_c)}\right) \\ &= \tilde{\mathbf{J}}_c^{-1}\left(\mathbf{r}_c\right) \frac{\partial \tilde{\mathbf{\Psi}}^{(2)}\left(\mathbf{r}_c\right)}{\partial \mathbf{r}_c}, \end{aligned} \tag{20}$$

where $\tilde{\mathbf{J}}_c\left(\mathbf{r}_c\right) = \frac{\partial \tilde{\mathbf{f}}_c^{(2)}(\mathbf{r}_c)}{\partial \mathbf{r}_c}$ and $\frac{\partial \tilde{\mathbf{\Psi}}^{(2)}}{\partial \mathbf{r}_c}$ are defined analogously to $\hat{\mathbf{J}}_p$ and $\frac{\partial \hat{\mathbf{N}}_p}{\partial \mathbf{r}_p}$. The presence of $\mathbf{f}_{cp}$ in (17) will affect the sensitivity analysis as seen shortly.

3. Optimization problem formulation and sensitivity analysis

A general finite-element-based shape optimization problem can be specified as [14]

$$\begin{aligned} &\min_{\mathbf{d}} g\left(\mathbb{U}(\mathbf{X}(\mathbf{d}), \mathbf{d}),\ \mathbf{X}(\mathbf{d}),\ \mathbf{d}\right), \\ &\text{such that: } h_j\left(\mathbb{U}(\mathbf{X}(\mathbf{d})),\ \mathbf{X}(\mathbf{d}),\ \mathbf{d}\right) \leq 0, \\ &\qquad\qquad \text{with } j = 1,\ 2,\ \ldots,\ l, \\ &\text{and} \quad \mathbb{K}\left(\mathbf{X}(\mathbf{d})\right)\mathbb{U}\left(\mathbf{X}(\mathbf{d}), \mathbf{d}\right) = \mathbb{F}\left(\mathbf{X}(\mathbf{d})\right), \end{aligned} \tag{21}$$

where g is the cost or objective function to minimize, h_j denotes the constraint functions, $\mathbf{X}$ denotes the nodal coordinate vector, and $\mathbf{d}$ is the design variable vector. Note that $\mathbf{X}$, $\mathbb{K}$, $\mathbb{U}$ and $\mathbb{F}$ are all functions of $\mathbf{d}$.

To perform a gradient-based optimization, a sensitivity analysis is needed to compute the gradients of objective and constraint functions with respect to the shape design variables. In the current study, the design variables are the geometrical parameters that define the material interfaces Γ_i. For instance, in an inclusion design problem with circular particles embedded in a matrix, the radius and center coordinates of the inclusions can serve as the shape design variables. Finite-element-based shape optimization presents two key challenges: (i) evaluating the mapping $\mathbf{X}$ from the design space to the node coordinate space, and (ii) computing the design velocity field, i.e., the derivative $\partial\mathbf{X}(\mathbf{d})/\partial\mathbf{d}$ for sensitivity analysis [14].

The sensitivity analysis of the cost and constraint functions is conducted by using an analytical discrete derivatives approach based on the direct and adjoint methods. Indeed, following the direct differential sensitivity analysis, the sensitivity of objective function expressed in (21) is obtained as

$$\frac{dg}{dd_i} = \left(\frac{\partial g}{\partial \mathbb{U}}\right)^T \overset{\star}{\mathbb{U}}_i + \left(\frac{\partial g}{\partial \mathbf{X}}\right)^T \mathbb{V}_i + \frac{\partial g}{\partial d_i} \tag{22}$$

where the partial derivatives of $\frac{\partial g}{\partial \mathbb{U}}$, $\frac{\partial g}{\partial \mathbf{X}}$, and $\frac{\partial g}{\partial d_i}$ are explicitly evaluated and the shape material derivative $\overset{*}{\mathbb{U}}_i = \frac{\partial \mathbb{U}}{\partial d_i}$ is computed in the pseudo analysis.

In the pseudo analysis the discrete linear system of equation (4) associated with the primal problem is differentiated with respect to each of the shape design variables d_i, resulting in a series of pseudo problems

$$\mathbb{K}\overset{*}{\mathbb{U}}_i = \mathbb{P}^i_{ps}, \tag{23}$$

where $\mathbb{P}^i_{ps}$ is the pseudo-load vector defined as

$$\mathbb{P}^i_{ps} = \frac{\partial \mathbb{F}}{\partial d_i} - \frac{\partial \mathbb{K}}{\partial d_i}\mathbb{U}. \tag{24}$$

The terms entering (24) are computed by assembling the element quantities:

$$\frac{\partial \mathbf{K}^e}{\partial d_i} = \begin{bmatrix} \mathbf{M}_{11} & \mathbf{M}_{12} \\ \mathbf{M}_{21} & \mathbf{M}_{22} \end{bmatrix} + \int_{\Omega_e} \mathbb{B}^T \mathbb{D}\mathbb{B}\, \mathrm{div}(\mathbb{V}_i)\, d\Omega, \tag{25}$$

$$\frac{\partial \mathbf{F}^e}{\partial d_i} = \int_{\Omega_e} \left[\frac{\partial \mathbb{N}^T}{\partial d_i} Q + \mathbb{N}^T \left(\overset{*}{Q}_i + Q\ \mathrm{div}\,(\mathbb{V}_i)\right)\right] d\Omega + \int_{\Gamma_e \cap S^q} \left[\frac{\partial \mathbb{N}^T}{\partial d_i} q + \mathbb{N}^T \left(\overset{*}{q}_i + q\ \mathrm{div}_\Gamma\,(\mathbb{V}_i)\right)\right] d\Gamma. \tag{26}$$

In (26), $\overset{*}{Q}_i$ and $\overset{*}{q}_i$ denote the material derivatives of heat source and heat flux with respect to d_i, respectively, while div and div_Γ are the divergence and surface divergence, defined below (see Eqs. (30) and (31)). The $\mathbf{M}_{ij}$ matrices entering (25) are defined as

$$\begin{aligned}
\mathbf{M}_{11} &= \sum_{j=1}^{2} \int_{\Omega_e^{(j)}} \left[\mathbf{B}_N^T \mathbb{D} \frac{\partial \mathbf{B}_N}{\partial d_i} + \mathbf{B}_N^T \overset{*}{\mathbb{D}}\, \mathbf{B}_N + \frac{\partial \mathbf{B}_N^T}{\partial d_i} \mathbb{D}\mathbf{B}_N\right] d\Omega, \\
\mathbf{M}_{12} = \mathbf{M}_{21}^T &= \sum_{j=1}^{2} \int_{\Omega_e^{(j)}} \left[\mathbf{B}_N^T \mathbb{D} \frac{\partial \mathbf{B}_\psi}{\partial d_i} + \mathbf{B}_N^T \overset{*}{\mathbb{D}}\, \mathbf{B}_\psi + \frac{\partial \mathbf{B}_N^T}{\partial d_i} \mathbb{D}\mathbf{B}_\psi\right] d\Omega, \\
\mathbf{M}_{22} &= \sum_{j=1}^{2} \int_{\Omega_e^{(j)}} \left[\mathbf{B}_\psi^T \mathbb{D} \frac{\partial \mathbf{B}_\psi}{\partial d_i} + \mathbf{B}_\psi^T \overset{*}{\mathbb{D}}\, \mathbf{B}_\psi + \frac{\partial \mathbf{B}_\psi^T}{\partial d_i} \mathbb{D}\mathbf{B}_\psi\right] d\Omega.
\end{aligned} \tag{27}$$

where $\overset{*}{\mathbb{D}}$ is the material derivative of $\mathbb{D}$ which we assume is zero hereafter.

The design velocity field $\mathbb{V}_i$ entering (25)–(26) must only be computed for the enriched elements. Considering Fig. 3 and (13), $\mathbb{V}_i$ in the integration element $\Omega_e^{(2)}$ is evaluated as the row vector

$$\mathbb{V}_i\left(\mathbf{X}\right)|_{\mathbf{X}=\tilde{\mathbf{f}}_c^{(2)}(\mathbf{r}_c,\mathbf{d})} = \frac{\partial \mathbf{X}\left(\mathbf{d}\right)}{\partial d_i} = \frac{\partial \tilde{\mathbf{f}}_c^2\left(\mathbf{r}_c,\mathbf{d}\right)}{\partial d_i} = \tilde{\mathbf{N}}_c^{(2)}\left(\mathbf{r}_c\right)\frac{\partial \mathbf{X}_e^{(2)}\left(\mathbf{d}\right)}{\partial d_i} = \tilde{\mathbf{N}}_c^{(2)}\left(\mathbf{r}_c\right)\mathbb{V}_{ei}^{(2)}\left(\mathbf{d}\right), \tag{28}$$

where $\mathbb{V}_{ei}^{(2)}\left(\mathbf{d}\right) = \frac{\partial \mathbf{X}_e^{(2)}(\mathbf{d})}{\partial d_i}$ denotes the 4×2 nodal shape velocity matrix of integration element $\Omega_e^{(2)}$. Note that all the nodal velocities, except those of the enriched nodes E_1 and E_2 on the material interface, are zero. The spatial derivative of the design velocity,

$$\frac{\partial \mathbb{V}_i\left(\mathbf{X},\mathbf{d}\right)}{\partial \mathbf{X}}|_{\mathbf{X}=\tilde{\mathbf{f}}_c^{(2)}(\mathbf{r}_c)} = \mathbf{B}_c^{(2)}\left(\mathbf{X},\mathbf{d}\right)\mathbb{V}_{ei}^{(2)}\left(\mathbf{d}\right), \tag{29}$$

is a 2×2 matrix, which can be used to compute

$$\mathrm{div}\left(\mathbb{V}_i\right) = \mathrm{tr}\left(\frac{\partial \mathbb{V}_i}{\partial \mathbf{X}}\right), \tag{30}$$

and

$$\mathrm{div}_\Gamma\left(\mathbb{V}_i\right) = \mathrm{tr}\left[\left(\mathbf{I} - \mathbf{n}\mathbf{n}^T\right)\frac{\partial \mathbb{V}_i}{\partial \mathbf{X}}\right], \tag{31}$$

where $\mathbf{n}$ is the outward unit normal vector to Γ. In the above $\mathbf{B}_c^{(2)}\left(\mathbf{X}\right)|_{\mathbf{X}=\tilde{\mathbf{f}}_c^{(2)}(\mathbf{r}_c)} = \tilde{\mathbf{J}}_c^{-1}\left(\mathbf{r}_c\right)\frac{\partial \tilde{\mathbf{N}}_c^{(2)}(\mathbf{r}_c)}{\partial \mathbf{r}_c}$ is defined analogously to $\mathbf{B}_\psi^{(2)}\left(\mathbf{X}\right)$, cf. (20).

By definition, $\mathbf{B}_N\left(\mathbf{r}_p\right) = \hat{\mathbf{J}}_p^{-1}\left(\mathbf{r}_p\right)\frac{\partial \hat{\mathbf{N}}_p(\mathbf{r}_p)}{\partial \mathbf{r}_p}$. Since both the Jacobian $\hat{\mathbf{J}}_p$ defined in (19) and the derivatives of the shape functions $\frac{\partial \hat{\mathbf{N}}_p(\mathbf{r}_p)}{\partial \mathbf{r}_p}$ are constant for the three-node triangular elements used in this study, $\frac{\partial \mathbf{B}_N}{\partial d_i}$, appearing in the bulk matrix $\mathbf{M}_{11}$ and $\mathbf{M}_{12}$ in (27) vanishes. However, the sensitivity $\frac{\partial \mathbf{B}_\psi}{\partial d_i}$ in each integration element, e.g., the integration element (2) in Fig. 3, is given by

$$\frac{\partial \mathbf{B}_\psi^{(2)}}{\partial d_i} = \frac{\partial \tilde{\mathbf{J}}_c^{-1}}{\partial d_i}\frac{\partial \tilde{\mathbf{\Psi}}^{(2)}}{\partial \mathbf{r}_c}, \tag{32}$$

where $\frac{\partial \tilde{\mathbf{J}}_c^{-1}}{\partial d_i}$ is obtained from

$$\frac{\partial \tilde{\mathbf{J}}_c^{-1}}{\partial d_i} = -\tilde{\mathbf{J}}_c^{-1}\frac{\partial \tilde{\mathbf{J}}_c}{\partial d_i}\tilde{\mathbf{J}}_c^{-1}, \tag{33}$$

with

$$\frac{\partial \tilde{\mathbf{J}}_c\left(\mathbf{r}_c,\mathbf{d}\right)}{\partial d_i} = \frac{\partial \tilde{\mathbf{N}}_c^{(2)}\left(\mathbf{r}_c\right)}{\partial \mathbf{r}_c}\mathbb{V}_{ei}^{(2)}\left(\mathbf{d}\right). \tag{34}$$

In (26), the $Q\mathrm{div}\left(\mathbb{V}_i\right)$ term is computed using (30) and we assume without loss of generality that the material derivative of the heat source, $\overset{*}{Q}_i$, is zero. Furthermore, we note that the last integral in (26) is zero for the internal boundary design problems investigated in the present study. However, the $\frac{\partial \mathbb{N}^T}{\partial d_i}$ term in (26), i.e., the derivative of the shape functions with respect to the design variables, is not zero in this IGFEM study, as opposed to regular FEM. To clarify this point, let us derive this sensitivity. As seen in (15), the shape function vector $\mathbb{N}$ in an enriched element is defined in terms of $\hat{\mathbf{N}}_p$ and $\tilde{\mathbf{\Psi}}$ and is evaluated over the master integration element, e.g., at location $\mathbf{r}_c$ in $\tilde{\Omega}_c^{(2)}$ in Fig. 3. The enriched shape function $\tilde{\mathbf{\Psi}}$ is independent of $\mathbf{d}$. Therefore, the derivatives of $\tilde{\mathbf{\Psi}}$ with respect to the

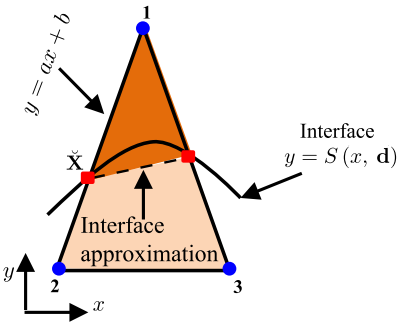

Fig. 4. Schematic of intersection of a material interface with the edges of non-conforming mesh.

design variables vanish, cf. the discussion following (15). On the other hand, $\hat{\mathbf{N}}_p \circ \mathbf{f}_{cp}$ is not independent of the design variables. Therefore, the derivative $\frac{\partial \mathbf{N}(\mathbf{X})}{\partial d_i}$ is not zero. Using Fig. 3 and (17), the sensitivity $\frac{\partial \mathbf{N}(\mathbf{X})}{\partial d_i}$ can be obtained as

$$
\begin{aligned}
\left.\frac{\partial \mathbf{N}\left(\hat{\mathbf{f}}_p\left(\mathbf{r}_p\right)\right)}{\partial d_i}\right|_{\mathbf{r}_p=\mathbf{f}_{cp}(\mathbf{r}_c)} &= \left.\frac{\partial \hat{\mathbf{N}}\left(\mathbf{r}_p\right)}{\partial d_i}\right|_{\mathbf{r}_p=\mathbf{f}_{cp}(\mathbf{r}_c,\,\mathbf{d})} \\
&= \frac{\partial \mathbf{f}_{cp}\left(\mathbf{r}_c,\,\mathbf{d}\right)}{\partial d_i} \left.\frac{\partial \hat{\mathbf{N}}\left(\mathbf{r}_p\right)}{\partial \mathbf{r}_p}\right|_{\mathbf{r}_p=\mathbf{f}_{cp}(\mathbf{r}_c,\,\mathbf{d})} \\
&= \frac{\partial \tilde{\mathbf{f}}_c\left(\mathbf{r}_c,\,\mathbf{d}\right)}{\partial d_i} \left.\frac{\partial \hat{\mathbf{f}}_p^{\downarrow}\left(\mathbf{X}\right)}{\partial \mathbf{X}}\right|_{\mathbf{X}=\tilde{\mathbf{f}}_c(\mathbf{r}_c,\,\mathbf{d})} \left.\frac{\partial \hat{\mathbf{N}}\left(\mathbf{r}_p\right)}{\partial \mathbf{r}_p}\right|_{\mathbf{r}_p=\mathbf{f}_{cp}(\mathbf{r}_c,\,\mathbf{d})} \\
&= \frac{\partial \tilde{\mathbf{f}}_c\left(\mathbf{r}_c,\,\mathbf{d}\right)}{\partial d_i} \left[\frac{\partial \hat{\mathbf{f}}_p\left(\mathbf{r}_p\right)}{\partial \mathbf{r}_p}\right]^{-1}\Bigg|_{\mathbf{r}_p=\mathbf{f}_{cp}(\mathbf{r}_c,\,\mathbf{d})} \left.\frac{\partial \hat{\mathbf{N}}\left(\mathbf{r}_p\right)}{\partial \mathbf{r}_p}\right|_{\mathbf{r}_p=\mathbf{f}_{cp}(\mathbf{r}_c,\,\mathbf{d})} \\
&= \mathbb{V}_i \hat{\mathbf{J}}_p^{-1} \left.\frac{\partial \hat{\mathbf{N}}}{\partial \mathbf{r}_p}\right|_{\mathbf{r}_p=\mathbf{f}_{cp}(\mathbf{r}_c,\,\mathbf{d})} \\
&= \mathbb{V}_i \mathbf{B}_N \,|_{\mathbf{r}_p=\mathbf{f}_{cp}(\mathbf{r}_c,\,\mathbf{d})}
\end{aligned}
\tag{35}
$$

where we use the fact that $\frac{\partial \hat{\mathbf{f}}_p^{\downarrow}}{\partial d_i}$ is zero.

Although a similar analytical sensitivity analysis was performed for the G/XFEM in [31], to the best of our knowledge, this is the first time that the sensitivity of the shape functions with respect to design parameters is introduced and computed. The correct extraction of the shape sensitivity in G/XFEM and IGFEM requires the inclusion of this term.

To complete the pseudo analysis of (23), it is necessary to compute the velocity field $\mathbb{V}_i$. In the IGFEM, the mesh is fixed and therefore only the enriched nodes on material interfaces move. Consequently, computing the enriched node velocity field suffices to complete the sensitivity analysis. The enriched nodes are added at the intersections of the material interfaces with the non-conforming element edges (Fig. 4). The intersection point $\breve{\mathbf{X}} = (\breve{x}, \breve{y})$ is found by solving the system of equations:

$$
\begin{cases}
\breve{y} = a\,\breve{x} + b \\
\breve{y} = S\left(\breve{x}, \mathbf{d}\right),
\end{cases}
\tag{36}
$$

where the first equation in (36) is the element edge equation, and the second one describes the material interface. The derivative of the above equation with respect to the design variable d_i gives the two components of the velocity of the

enriched node:

$$(V_x)_i = \frac{\frac{\partial S(\check{x},\mathbf{d})}{\partial d_i}}{a - \frac{\partial S(\check{x},\mathbf{d})}{\partial x}} \quad \text{and} \quad \left(V_y\right)_i = a\,(V_x)_i\,. \tag{37}$$

In the rare event that the material interface passes exactly through a node of the non-conforming mesh, (37) is not applicable. Two approaches can be considered in this situation: (i) introducing a very small perturbation in the design variable, or (ii) perturbing the location of that node in the background mesh. Both approaches have proven successful for our numerical studies. In our example problems we follow (ii).

Summarizing, in the direct differentiation sensitivity analysis for each parameter d_i we evaluate the pseudo load $\mathbb{P}^i_{ps}$ and solve (23) to evaluate the shape material derivative $\overset{*}{\mathbb{U}}_i$. Having the $\overset{*}{\mathbb{U}}_i$, we compute the sensitivity (22) for the cost and constraint functions.

Alternatively, the sensitivity of objective function can be evaluated using the adjoint method by annihilating $\overset{*}{\mathbb{U}}_i$ from (22). Regarding the adjoint method sensitivity analysis, for each function, e.g. g, we compute the adjoint response $\boldsymbol{\lambda}_g$ such that

$$\mathbb{K}\boldsymbol{\lambda}_g = \left(\frac{\partial g}{\partial \mathbb{U}}\right)^T, \tag{38}$$

and evaluate the sensitivity via

$$\frac{dg}{dd_i} = \left(\frac{\partial g}{\partial \mathbf{X}}\right)^T \mathbb{V}_i + \frac{\partial g}{\partial d_i} + \boldsymbol{\lambda}_g^T \mathbb{P}^i_{ps}, \tag{39}$$

where $\mathbb{P}^i_{ps}$ is defined in (24).

4. Algorithm

Based on the equations described in the previous section, the gradient-based IGFEM shape optimization algorithm can be summarized as follows:

1. Assign an initial guess for the design variables: $\mathbf{d} = \mathbf{d}_0$
   Loop until converged
2. Implement IGFEM
   (a) Find intersection points
   (b) Update mesh by adding new nodes at intersection points
   (c) Apply enrichments to intersected elements
3. Solve $\mathbb{K}\mathbb{U} = \mathbb{F}$ for nodal solution $\mathbb{U}$ (4)
4. Compute objective and constraint functions
5. Compute pseudo-load vector (24)
   (a) Compute interface node velocity field $\mathbb{V}$
   (b) Compute derivative of global stiffness matrix
   (c) Compute derivative of global load vector
6. Perform adjoint analysis (38)
7. Compute sensitivity of objective and constraint functions (39)
8. Update the design variables
   End Loop

To conclude the presentation of the shape optimization scheme, it is worth emphasizing that, like other gradient-based methods, one cannot guarantee convergence to a global optimum in the presence of multiple local optima. The analysis might therefore require the use of multiple initial guesses for the initial design. Once again, by avoiding the need to generate a conforming mesh for each starting geometry, the IGFEM approach greatly facilitates this process: only the mathematical description of the internal material interfaces is needed to define the model on the non-conforming stationary mesh [44].

5. Numerical examples

In this section, we apply the IGFEM shape optimization scheme to several 2D thermal and structural problems to verify and illustrate the proposed method. The first two examples are used as thermal and structural benchmarks for the current work. The third problem involves the shape optimization of a microvascular material for high temperature applications, while the last application optimizes the distribution of inclusions in a structurally loaded particulate composite.

5.1. Thermal verification problem: circular inclusion

In this first example, we consider the simple problem of a circular inclusion of radius R, with thermal conductivity κ_2 and distributed heat source Q_2 embedded in a square domain of size L (with thermal conductivity κ_1 and heat source Q_1) subjected to a heat flux q uniformly applied along its bottom edge (Fig. 5(a)). The left and right edges are insulated, while the top edge is kept at a fixed temperature T_0. The optimization problem consists of finding the inclusion radius R that maximizes the average temperature along the bottom edge $\bar{T}_b$. For the dimensions ($L = 0.1$ m), thermal loading ($q = 1000$ W/m^2, $T_0 = 20$°C, $Q_1 = 10$ W/m^3, and $Q_2 = 50{,}000$ W/m^3) and thermal properties ($\kappa_1 = 17$ W/mK and $\kappa_2 = 100$ W/mK), $\bar{T}_b$ reaches a maximum of 26.82°C at $R/L = 0.31$, as shown in Fig. 5(g).

Fig. 5(b) and (c) illustrate the application of the IGFEM shape optimization scheme to this verification problem, starting from an initial value of the inclusion radius $R/L = 0.1$, as indicated by the blue contours intersection points in Fig. 5(b). The red dots on the same figure denote the converged shape of the inclusion and the resulting thermal field is presented in Fig. 5(c). The convergence history is shown by the solid curves in Fig. 5(h), with the blue curve denoting the evolution of $\bar{T}_b$ and the green curve that of the ratio R/L. As apparent there, the optimal solution rapidly converges to the aforementioned exact values (denoted by the dotted horizontal lines).

For comparison, Fig. 5(d)–(f) illustrate the solution of the same shape optimization problem using a conventional finite element scheme with meshes that conform to the evolving particle size, starting again from an initial guess $R/L = 0.1$ (Fig. 5(d)). As the particle size increases, the elements inside the particle are stretched, while those outside the inclusion undergo substantial distortions, which leads to a loss of precision as shown by the dashed curves in Fig. 5(h). This simple example illustrates the key advantage of the proposed method that relies on a fixed non-conforming mesh.

5.2. Structural verification problem: elliptical inclusion

In this second verification problem, we optimize the shape of an elliptical inclusion embedded in a matrix to minimize the compliance subject to a prescribed inclusion area constraint. The problem is solved in plane strain and the square domain (of size L) is subjected to a uniform traction σ_0 along its top edge, while 'roller boundary conditions' are assumed along the bottom edge as depicted in Fig. 6(a). The matrix is stiffer than the inclusion with material properties $E_1/E_2 = 10$ and $\nu_1 = \nu_2$. The design variables are the size of the major a and minor b axes of the ellipse, and the inclusion area constraint is $ab = 0.02L^2$. The range of the minor and major radii are $0.1L \leq a, b \leq 0.2L$. This example resembles a classical benchmark for shape optimization in which the axis lengths and orientation of an elliptical inclusion of area A embedded in an infinite media are optimized to minimize compliance. The analytical solution requires that the axes be aligned with the far-field principle strain directions and that the ratio of the semi-major axis to semi-minor axis equals the ratio of the far-field principle strains [45]. In our example, since the loading is uniaxial, the matrix and inclusion are isotropic and there are constraints for the range of the minor and major radii for a constant area, the optimal shape of a compliant elliptical inclusion embedded in a stiff matrix is expected to be an ellipse with the major axis in the direction of far-field stress. The results illustrated in Fig. 6(b) show that, starting from an initial guess $a/L = 2b/L = 0.2$ (yellow outline in Fig. 6(c)), the solution converges in less than 20 iterations to the expected optimum design $2a/L = b/L = 0.2$ (red outline in Fig. 6(c)). The von Mises stress distributions associated with the initial and optimal designs are plotted on their respective deformed configurations in Fig. 6(d) and (e).

5.3. Thermal application: microvascular materials

In [44,46], the results of a parametric design of an actively cooled woven microvascular composite plate with sinusoidal and straight microchannels were summarized. In this third problem, we use the IGFEM-based shape

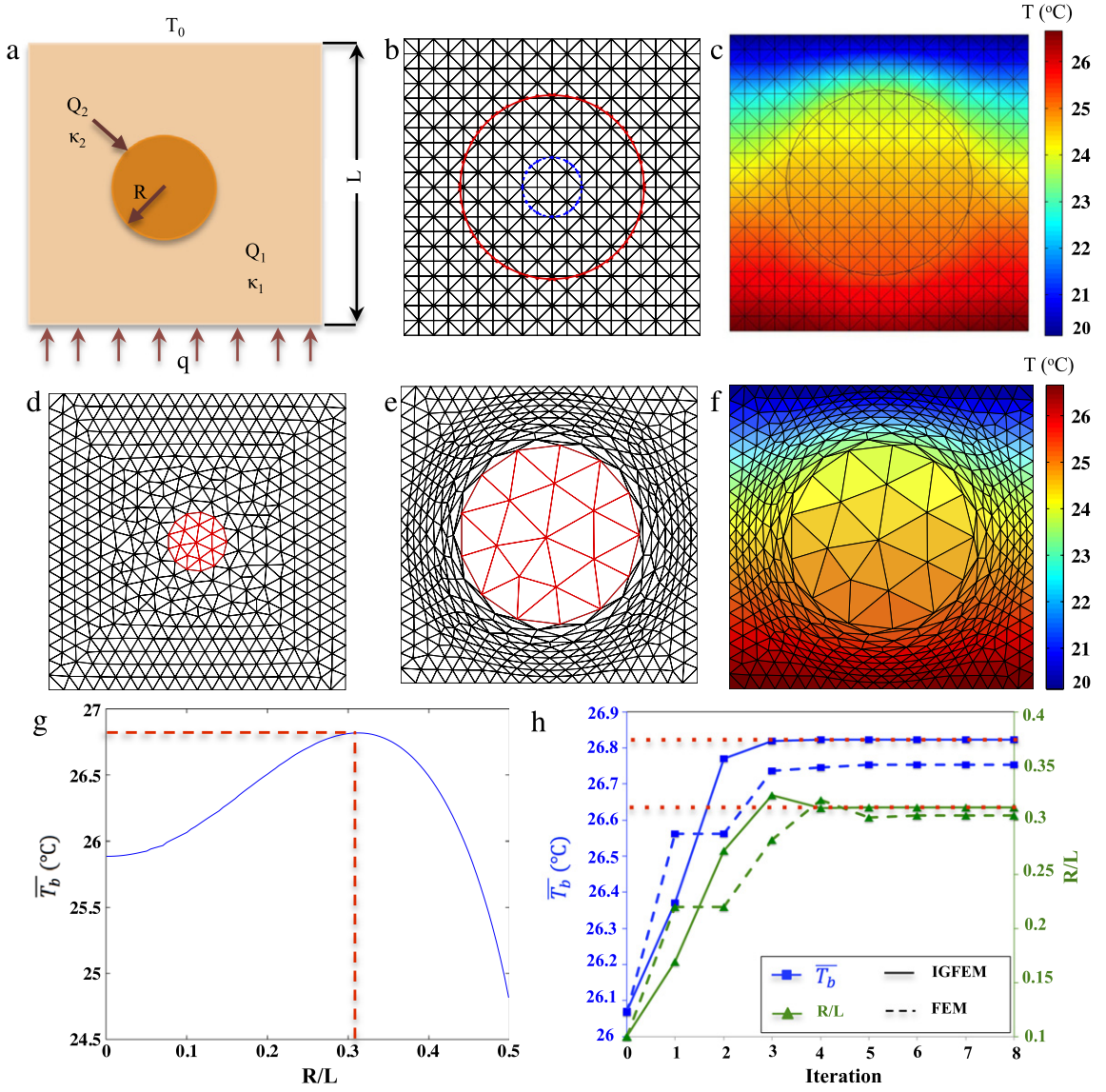

Fig. 5. Comparison between conventional FEM vs. IGFEM-based shape optimization (a) Problem description; (b) Initial (blue) and optimum (red) shapes, and (c) optimal temperature field for the IGFEM approach; Initial (d), optimum shape (e), and optimal temperature field (f) for the conventional FEM scheme; (g) $\bar{T}_b$ vs. R solution obtained through a parametric numerical study, showing a maximum value at $R/L = 0.31$; (h) Design convergence history, with the dotted horizontal curves denoting the exact optimal values of the average temperature and inclusion radius given in (g). (For interpretation of the references to color in this figure legend, the reader is referred to the web version of this article.)

optimization scheme to investigate the similar (though simpler) 2D problem shown in Fig. 7, wherein fluid flows through a sinusoidal microchannel (of fixed diameter $d = 500$ μm) defined by its wavelength $\lambda = 1$ cm and amplitude A to cool a rectangular domain of length $L = 10$ cm and height $H = 6$ mm. The goal of the design is to optimize the amplitude A to minimize the average temperature on the bottom edge ($\bar{T}_b$).

The domain is subjected to a uniform heat flux $q = 10$ kW/m^2 applied along its bottom edge, while a Dirichlet boundary condition ($T_0 = 20$°C) is applied along the top boundary. The microvascular medium is made of epoxy ($\kappa = 0.45$ W/m.K). Cooling is achieved by pumping water ($\kappa = 0.6$ W/m.K, $\rho = 1000$ kg/m^3, $c_p = 4183$ J/kgK) through the channel with a flow rate Q and an inlet temperature $T_{inlet} = 20$°C. The centerline locations for the inlet and outlet are set at a distance d from the lower edge. Assuming fully developed Poiseuille flow conditions, the

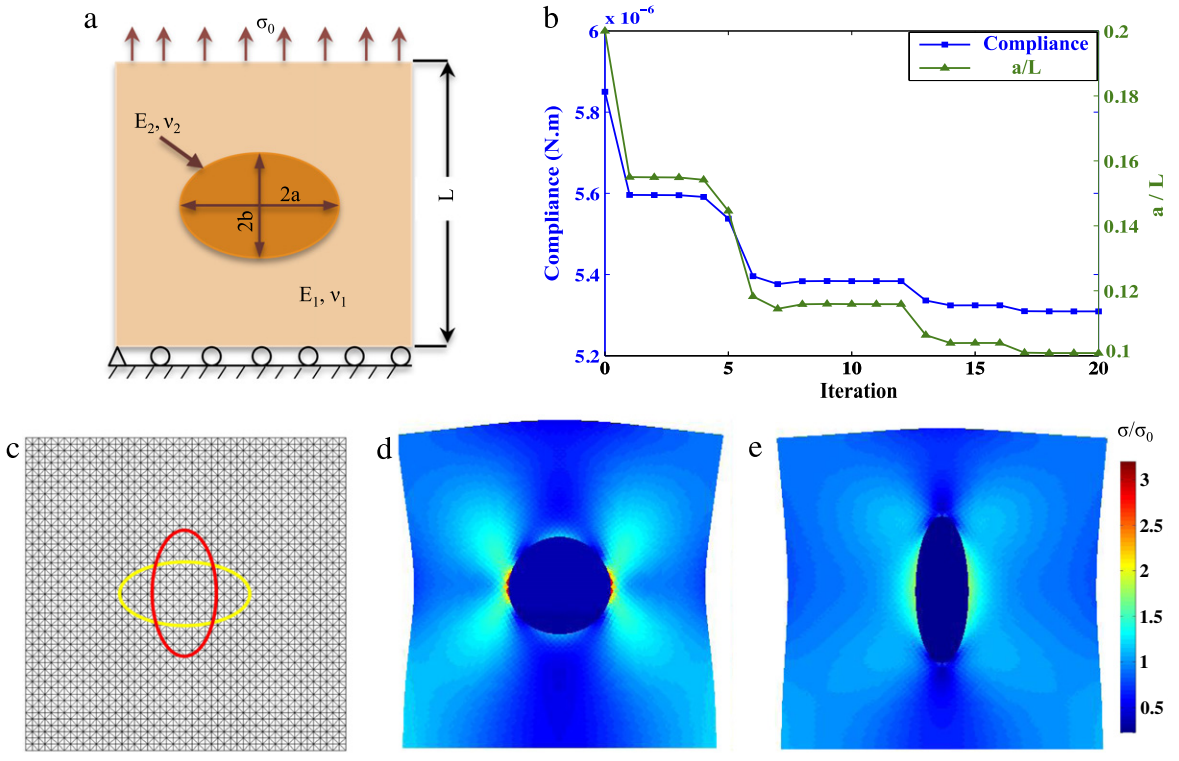

Fig. 6. Shape optimization for a compliant elliptical inclusion embedded in a stiff matrix: (a) Problem description; (b) Convergence and design history; (c) Initial (yellow outline) and optimum (red outline) designs; (d) and (e) von Mises stress distributions corresponding to the initial and optimum designs over the deformed configurations, with the displacements scaled by $0.26 \times E_2/\sigma_0$. (For interpretation of the references to color in this figure legend, the reader is referred to the web version of this article.)

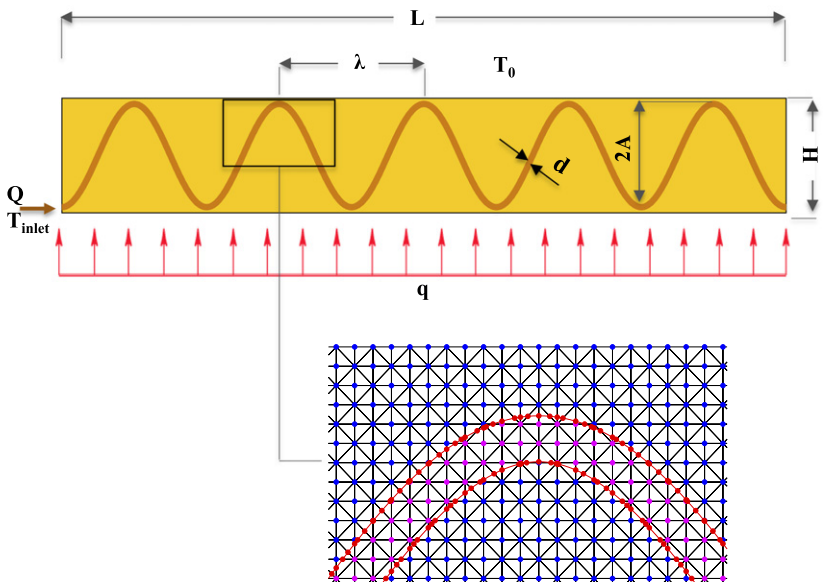

Fig. 7. Shape optimization of a sinusoidal microchannel embedded in a rectangular domain: problem geometry and thermal loading conditions. The lower figure shows details of the non-conforming finite element mesh used in the IGFEM analysis.

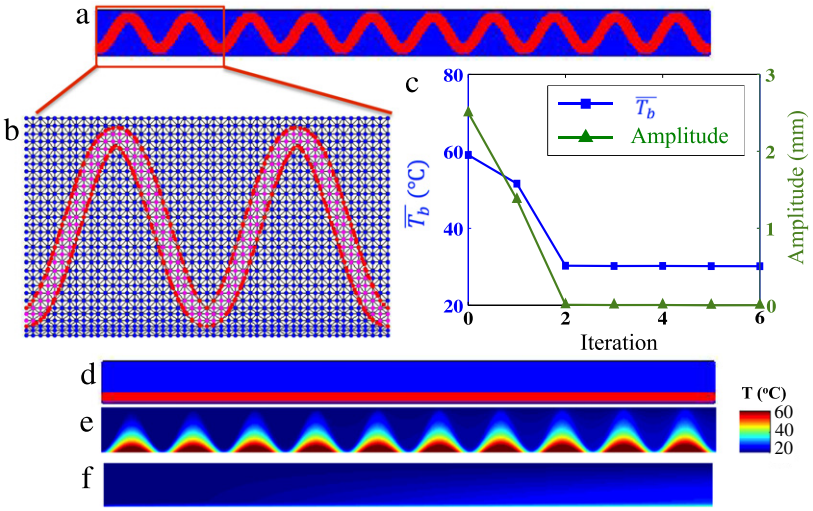

Fig. 8. Shape optimization for sinusoidal microchannel shown in Fig. 7 with flow rate $Q = 1$ ml/min: (a) Initial design; (b) Magnified view with non-conforming mesh; (c) Convergence history of the average temperature along the bottom edge ($\bar{T}_b$) and of the microchannel amplitude (A); (d) Optimal design; (e) and (f) Initial and optimal temperature distributions.

velocity profile over the cross section of the sinusoidal microchannel is expressed as [47]

$$\mathbf{V} = V_{\max}\left[1 - \left(\frac{r}{d/2}\right)^2\right]\mathbf{e}_t, \tag{40}$$

where $V_{\max} = 8Q/\pi d^2$ is the maximum velocity of the coolant, r is the distance from the microchannel centerline and $\mathbf{e}_t$ is the tangent vector directed along the center line. The cooling is modeled by adding the convective term $\mathbf{K}^e_{conv} = \int_{\Omega_e} \mathbb{N}^T \rho c_p \mathbf{V}\mathbb{B}\, d\Omega$ to the microchannel element stiffness matrices and its derivative to (25). Details on the finite element formulation for this problem can be found in [32].

As shown in [44] and [46], the optimum configuration of the microchannel depends on the flow rate Q: for low flow rate values, the optimum solution corresponds to a wavy microchannel with maximum amplitude A, while, at higher flow rates, a straight microchannel ($A = 0$) located close to the lower (hot) edge is most effective at cooling the domain. In an attempt to reproduce these results using the proposed gradient-based IGFEM shape optimization scheme, we aim to find the optimum value of A. The allowable range for A is chosen to be bounded by $0 \le A \le A_{\max} = \left(\frac{H}{2} - d\right)$ such that the centerline of the microchannel is at least a distance d of the upper and lower edges.

The solution corresponding to a higher flow rate value ($Q = 1$ ml/min) is presented in Fig. 8. Starting from an initial guess corresponding to the maximum allowable value for the microchannel amplitude ($A = 2.5$ mm, Fig. 8(a)), the optimizer converges to the optimal configuration with a straight microchannel (Fig. 8(d)) in two iterations (Fig. 8(c)). As shown in Fig. 8(c), the average temperature along the bottom edge of the domain reduces from 59°C to about 30°C. The temperature fields for the initial and optimal designs are presented in Fig. 8(e) and (f).

To study the aforementioned impact of the flow rate on the optimum shape of the microchannel, we repeat the example with $Q = 0.05$ ml/min, starting from $A = A_{\max}/2$. In contrast with the results obtained for $Q = 1$ ml/min, the solution converges to the configuration with the maximum allowable amplitude. The results are illustrated in Fig. 9.

5.4. Structural application: particulate composites

In the example presented in this section, the design variables are the radii and locations of five circular inclusions (of stiffness E_2 and Poisson's ratio ν_2) embedded in a square linearly elastic plane strain plate (of length $L = 0.1$ m, stiffness $E_1 = E_2/10$ and Poisson's ratio $\nu_1 = \nu_2$) subjected to a linearly varying distributed traction applied along its upper edge (Fig. 10(a)). We minimize the compliance of the composite subject to a maximum inclusions area fraction

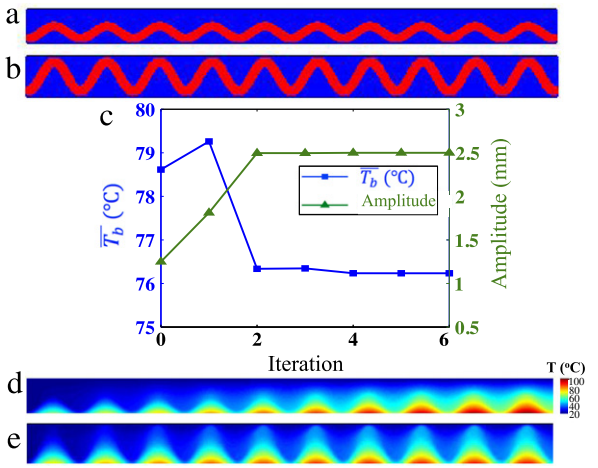

Fig. 9. Shape optimization for sinusoidal micro-channel shown in Fig. 7 with the lower flow rate $Q = 0.05$ ml/min: (a) and (b) Initial and optimal designs; (c) Convergence history of the average temperature along the bottom edge ($\bar{T}_b$) and of microchannel amplitude (A); (d) and (e) Initial and optimal temperature distributions.

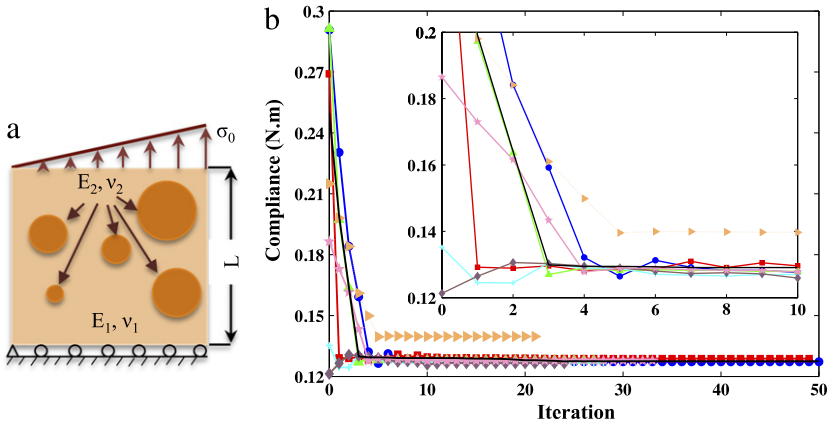

Fig. 10. (a) Problem description for a plate with five inclusions; (b) Convergence history of the structure compliance for eight different initial designs.

constraint ($A_f \leq 0.1125\pi$). To prevent overlapping, we also impose that the distance C_{ij} between inclusions i and j satisfy $C_{ij} \geq R_i + R_j + 0.03L$. The design variables are bounded as $0.03L \leq R_i \leq 0.2L$ and $0.2L \leq X_{ci}, Y_{ci} < 0.8L$.

The convergences histories of the compliance for eight trials with different initial designs are presented in Fig. 10(b). The figure shows that the convergences are stable and that all of the trials except one converge to very similar optimal values for compliance. The initial and final designs for four trials are illustrated in Fig. 11. As apparent there, the inclusions move to the right to minimize the compliance due to unsymmetrical loading.

6. Conclusions

A gradient-based shape optimization over a fixed mesh based on the recently introduced Interface-enriched Generalized Finite Element Method (IGFEM) has been developed, taking advantage of both Eulerian and Lagrangian approaches to eliminate mesh distortion issues as well as to represent geometrical features accurately. Furthermore, the analytical sensitivity analysis adapted in this work circumvents issues commonly encountered in finite difference and semi-analytical sensitivity approaches. By substantially simplifying the meshing process and avoiding remeshing, the proposed method also provides a very efficient way to simulate multiple initial configurations when searching for a global optimum.

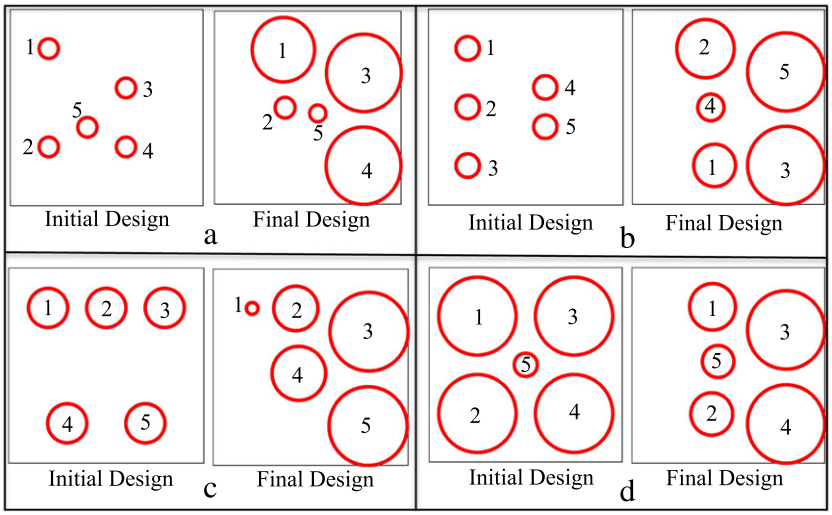

Fig. 11. Initial and optimal designs for the problem shown in Fig. 10 corresponding to four different initial designs.

The method has been verified with and applied to various 2D structural and thermal multi-inclusion and microvascular problems. The results have shown that the proposed method converges to the optimum solution accurately and efficiently.

Acknowledgments

This work has been supported by the Air Force Office of Scientific Research Multidisciplinary University Research Initiative under contract # FA9550-09-1-0686. Support for M. Safdari was provided through a Grant No. FA9550-12-1-0445 to the Center of Excellence on Integrated Materials Modeling (CEIMM) at Johns Hopkins University (partners JHU, UIUC, and UCSB) awarded by the AFOSR/RSL (Computational Mathematics Program, Manager Dr. F. Fahroo) and AFRL/RX (Monitors Dr. C. Woodward and T. Breitzman).

References

[1] J. Ródenas, F. Fuenmayor, J. Tarancón, A numerical methodology to assess the quality of the design velocity field computation methods in shape sensitivity analysis, Internat. J. Numer. Methods Engrg. 59 (13) (2004) 1725–1747.
[2] R.T. Haftka, R.V. Grandhi, Structural shape optimization—a survey, Comput. Methods Appl. Mech. Engrg. 57 (1) (1986) 91–106.
[3] J.D. Foley, A. van Dam, S. Feiner, J. Hughes, Computer Graphics, Principle, and Practice, second ed., 1990.
[4] S. Chen, D. Tortorelli, Three-dimensional shape optimization with variational geometry, Struct. Optim. 13 (2–3) (1997) 81–94.
[5] V. Braibant, C. Fleury, Shape optimal design using b-splines, Comput. Methods Appl. Mech. Engrg. 44 (3) (1984) 247–267.
[6] J. Bennett, M. Botkin, Structural shape optimization with geometric description and adaptive mesh refinement, AIAA J. 23 (3) (1985) 458–464.
[7] R. Yang, D. Dewhirst, J. Allison, A. Lee, Shape optimization of connecting rod pin end using a generic model, Finite Elem. Anal. Des. 11 (3) (1992) 257–264.
[8] D. Tortorelli, J. Tomasko, T. Morthland, J. Dantzig, Optimal design of nonlinear parabolic systems. Part II: Variable spatial domain with applications to casting optimization, Comput. Methods Appl. Mech. Engrg. 113 (1) (1994) 157–172.
[9] A. Belegundu, S. Rajan, A shape optimization approach based on natural design variables and shape functions, Comput. Methods Appl. Mech. Engrg. 66 (1) (1988) 87–106.
[10] D.A. Tortorelli, A geometric representation scheme suitable for shape optimization, Mech. Struct. Mach. 21 (1) (1993) 95–121.
[11] C. Mattheck, S. Burkhardt, A new method of structural shape optimization based on biological growth, Int. J. Fatigue 12 (3) (1990) 185–190.
[12] R. Meske, J. Sauter, E. Schnack, Nonparametric gradient-less shape optimization for real-world applications, Struct. Multidiscip. Optim. 30 (3) (2005) 201–218.
[13] K.-U. Bletzinger, M. Firl, J. Linhard, R. Wüchner, Optimal shapes of mechanically motivated surfaces, Comput. Methods Appl. Mech. Engrg. 199 (5–8) (2010) 324–333.
[14] C. Le, T. Bruns, D. Tortorelli, A gradient-based, parameter-free approach to shape optimization, Comput Methods Appl Mech Eng 200 (9) (2011) 985–996.
[15] N. Kim, Y. Chang, Eulerian shape design sensitivity analysis and optimization with a fixed grid, Comput Methods Appl Mech Eng 194 (30) (2005) 3291–3314.

[16] P. Duysinx, L. Van Miegroet, T. Jacobs, C. Fleury, Generalized shape optimization using X-FEM and level set methods, in: IUTAM Symposium on Topological Design Optimization of Structures, Machines and Materials, Springer, 2006, pp. 23–32.
[17] F. Bobaru, S. Rachakonda, E(FG)2: a new fixed-grid shape optimization method based on the element-free galerkin mesh-free analysis, Struct. Multidiscip. Optim. 32 (3) (2006) 215–228.
[18] G. Allaire, F. Jouve, A. Toader, Structural optimization using sensitivity analysis and a level-set method, J. Comput. Phys. 194 (1) (2004) 363–393.
[19] P. Dunning, H. Kim, G. Mullineux, Investigation and improvement of sensitivity computation using the area-fraction weighted fixed grid FEM and structural optimization, Finite Elem. Anal. Des. 47 (8) (2011) 933–941.
[20] I. Grindeanu, K. Choi, J. Chen, K. Chang, Shape design optimization of hyperelastic structures using a meshless method, AIAA J. 37 (8) (1999) 990–997.
[21] F. Bobaru, S. Rachakonda, Boundary layer in shape optimization of convective fins using a meshfree approach, Int J Numer Methods Eng 60 (7) (2004) 1215–1236.
[22] J. Haslinger, J. Maitre, L. Tomas, Fictitious domains methods with distributed lagrange multipliers Part II: application to the solution of shape optimization problems, Math. Methods Appl. Sci. 11 (03) (2001) 549–563.
[23] J. Norato, R. Haber, D. Tortorelli, M. Bendsøe, A geometry projection method for shape optimization, Int J Numer Methods Eng 60 (14) (2004) 2289–2312.
[24] D. Wang, W. Zhang, A general material perturbation method using fixed mesh for stress sensitivity analysis and structural shape optimization, Comput. Struct. 129 (2013) 40–53.
[25] X. Wang, M.Y. Wang, D. Guo, Structural shape and topology optimization in a level-set-based framework of region representation, Struct. Multidiscip. Optim. 27 (1–2) (2004) 1–19.
[26] P. Wei, M. Wang, X. Xing, A study on X-FEM in continuum structural optimization using a level set model, Comput. Aided Des. 42 (8) (2010) 708–719.
[27] L. Van Miegroet, N. Moës, C. Fleury, P. Duysinx, Generalized shape optimization based on the level set method, in: Proceedings of the 6th World Congress of Structural and Multidisciplinary Optimization (WCSMO6), 2005.
[28] L. Van Miegroet, P. Duysinx, Stress concentration minimization of 2D filets using X-FEM and level set description, Struct. Multidiscip. Optim. 33 (4–5) (2007) 425–438.
[29] Z. Luo, M. Wang, S. Wang, P. Wei, A level set-based parameterization method for structural shape and topology optimization, Int J Numer Methods Eng 76 (1) (2008) 1–26.
[30] M. Edke, K. Chang, Shape sensitivity analysis for 2D mixed mode fractures using extended FEM (XFEM) and level set method (LSM)#, Mech. Des. Struct. Mach. 38 (3) (2010) 328–347.
[31] J. Zhang, W. Zhang, J. Zhu, L. Xia, Integrated layout design of multi-component systems using XFEM and analytical sensitivity analysis, Comput. Methods Appl. Mech. Engrg. 245 (2012) 75–89.
[32] S. Soghrati, A. Aragón, C. Duarte, P. Geubelle, An interface-enriched generalized finite element method for problems with discontinuous gradient fields, Int J Numer Methods Eng 89 (8) (2012) 991–1008.
[33] S. Soghrati, P. Geubelle, A 3D interface-enriched generalized finite element method for weakly discontinuous problems with complex internal geometries, Comput Methods Appl Mech Eng 217–220 (2012) 46–57.
[34] T. Yao, K. Choi, 3D shape optimal design and automatic finite element regridding, Int J Numer Methods Eng 28 (2) (1989) 369–384.
[35] K. Choi, K. Chang, A study of design velocity field computation for shape optimal design, Finite Elem. Anal. Des. 15 (4) (1994) 317–341.
[36] T. Lindby, J. Santos, 2D and 3D shape optimization using mesh velocities to integrate analytical sensitivities with associative CAD, Struct. Optim. 13 (4) (1997) 213–222.
[37] D. Tortorelli, W. Zixian, A systematic approach to shape sensitivity analysis, Int. J. Solids Struct. 30 (9) (1993) 1181–1212.
[38] F. Van Keulen, R. Haftka, N. Kim, Review of options for structural design sensitivity analysis. Part 1: Linear systems, Comput. Methods Appl. Mech. Engrg. 194 (30) (2005) 3213–3243.
[39] T. Belytschko, R. Gracie, G. Ventura, A review of extended/generalized finite element methods for material modeling, Model. Simul. Mater. Sci. Eng. 17 (4) (2009) 043001.
[40] I. Babuška, U. Banerjee, Stable generalized finite element method (SGFEM), Comput. Methods Appl. Mech. Engrg. 201 (2012) 91–111.
[41] A. Düster, J. Parvizian, Z. Yang, E. Rank, The finite cell method for three-dimensional problems of solid mechanics, Comput. Methods Appl. Mech. Engrg. 197 (45) (2008) 3768–3782.
[42] D. Schillinger, M. Ruess, N. Zander, Y. Bazilevs, A. Düster, E. Rank, Small and large deformation analysis with the p- and b-spline versions of the finite cell method, Comput. Mech. 50 (4) (2012) 445–478.
[43] M. Ruess, D. Schillinger, A.I. Özcan, E. Rank, Weak coupling for isogeometric analysis of non-matching and trimmed multi-patch geometries, Comput. Methods Appl. Mech. Engrg. 269 (2014) 46–71.
[44] S. Soghrati, A. Najafi, J. Lin, K. Hughes, S. White, N. Sottos, P. Geubelle, Computational analysis of actively-cooled 3D woven microvascular composites using a stabilized interface-enriched generalized finite element method, Int. J. Heat Mass Transfer 65 (2013) 153–164.
[45] V. Kobelev, "bubble-and-grain" method and criteria for optimal positioning inhomogeneities in topological optimization, Struct. Multidiscip. Optim. 40 (1–6) (2010) 117–135.
[46] A. Najafi, S. Soghrati, N. Sottos, S. White, P. Geubelle, Computational design of actively-cooled microvascular composite skin panels for hypersonic aircraft, in: Proceedings of the 54th AIAA/ASME/ASCE/AHS/ASC Structures, Structural Dynamics, and Materials Conferences, 2013.
[47] C. Brebbia, A. Ferrante, Computational Hydraulics, Butterworths, 1983.